Journal of Materials Chemistry A

ROYAL SOCIETY OF CHEMISTRY

PAPER

View Article Online
View Journal | View Issue

Cite this: J. Mater. Chem. A, 2020, 8, 5171

$Ti_3C_2T_x$ MXene decorated black phosphorus nanosheets with improved visible-light photocatalytic activity: experimental and theoretical studies†

Binbin Shao,‡ Jiajia Wang,‡ Zhifeng Liu, * Guangming Zeng, * Lin Tang, Qinghua Liang, Qingyun He, Ting Wu, Yang Liu and Xingzhong Yuan

Received 12th December 2019
Accepted 1st February 2020

DOI: 10.1039/c9ta13610j

rsc.li/materials-a

Metal-free black phosphorus (BP) nanosheets have emerged as a promising photocatalyst. Herein, early transition-metal carbide and nitride (MXene) decorated BP ($Ti_3C_2T_x/TiO_2$–BP) nanohybrids were constructed by a hydrothermal method, in which TiO_2 was produced in the hydrothermal process. The optimized $Ti_3C_2T_x/TiO_2$–BP nanohybrids exhibited a higher visible-light photodegradation efficiency of rhodamine B (99.09%) and tetracycline hydrochloride (92.70%) pollutants than that of pristine BP (12.75% and 9.35%, respectively). Diverse characterization techniques and density functional theory calculations have revealed that such enhanced photocatalytic performance was due to the synergistic effect of BP and $Ti_3C_2T_x/TiO_2$, which could markedly improve the stability of BP, increase visible light absorption, prolong the photoexcited electron lifetime, accelerate the photoinduced electron transfer and hinder the electron–hole (e^-–h^+) pair recombination. Meanwhile, the mechanism analysis indicated that $^{\bullet}O_2^-$ radicals played a leading role in the photocatalytic process. This study will motivate great interest in using 2D MXenes as co-catalysts to enhance the activity of BP for its applications.

1. Introduction

With the rapid development of society, the energy crisis and environmental pollution have brought great challenges to mankind.[1–4] Photocatalysis is one of the most convenient and promising approaches to overcome these challenges.[5,6] Since Fujishima and Honda first reported the phenomenon of photocatalytic water splitting by TiO_2 under UV-light illumination in 1972,[7] hitherto, hundreds of photocatalysts (*e.g.* g-C_3N_4, CdS, Bi_2WO_6, TiO_2, Ag_3PO_4, MOFs, *etc.*[8–13]) have been investigated for multifunctional photocatalytic applications, including H_2 generation, O_2 reduction, CO_2 reduction, pollutant degradation, antibacterial, *etc.*[14–18] However, some drawbacks, such as, insufficient use of light, quick recombination of photogenerated e^-–h^+ pairs, and photocorrosion, limit their practical application.[19–22] Therefore, to develop efficient photocatalysts with excellent performance is still urgent.

Black phosphorus (BP), a new metal-free layered 2D crystal material, is constructed using only one kind of element and can be exfoliated from bulk crystals through breaking the van der Waals forces between them.[23–25] Since the successful production of 2D BP with atom-thick layers in 2014, it has received tremendous attention lately due to its satisfactory optoelectronic and physicochemical properties.[26–28] Theoretical and experimental studies have shown that the band gap of BP could be adjusted from 0.3 eV to 2.1 eV depending on its thickness (bulk to monolayer).[29] BP exhibits high carrier mobility, remarkable in-plane anisotropic electronic properties, and excellent light absorption capacity in both visible and near-infrared regions.[30–33] However, there are some intrinsic defects in BP nanosheets, which cause a big obstacle for their practical application. For instance, exfoliated BP is very sensitive to moisture and ambient oxygen, and will be readily oxidized due to the uncovered lone pairs on its surface. Meanwhile, the roughness resulting from the exfoliation will further accelerate the surface oxidation, thus the semiconducting properties and photocatalytic performance deteriorate rapidly limiting the practical application of BP.[34–36] It is important to develop effective BP stabilization techniques, thus reducing or eliminating the degradation of BP. Recently, several strategies have been studied to prevent BP from oxidation, among them, the construction of heterostructures between BP and other co-catalysts was proposed as an effective method. For instance, Zhang *et al.*[31] designed a 2D/2D g-C_3N_4/BP heterostructure exhibiting a high H_2 generation rate (reaching 384.17 μmol g^{-1} h^{-1}) under visible-light illumination. In addition, diverse BP-

College of Environmental Science and Engineering, Key Laboratory of Environmental Biology and Pollution Control, Hunan University, Ministry of Education, Changsha 410082, P. R. China. E-mail: zhifengliu@hnu.edu.cn; zgming@hnu.edu.cn

† Electronic supplementary information (ESI) available. See DOI: 10.1039/c9ta13610j

‡ These authors contributed equally to this article.

based heterostructures have been studied in the photocatalytic field, such as transition metal dichalcogenides (MoS_2, WS_2)/BP,[26,33,37] TiO_2/BP,[38] $BiVO_4$/BP,[39] Bi_2WO_6/BP,[40] and so on. The formation of nanohybrids leads to numerous active sites, higher conductivity, and increased light harvesting capability suppressing the oxidation of BP, thus improving the photocatalytic performance significantly.

Compared to other materials, early transition-metal carbides and nitrides (MXenes) as a new class of 2D materials have aroused great interest due to their high electrical conductivity, hydrophilicity, abundant active catalytic sites, easily tunable structure, and superior oxidation resistance.[41–43] Generally, they are obtained through etching "A" out of the MAX phase (M, A, and X is an early transition metal, a main group IIIA or IVA element, and a carbon and/or nitrogen atom, respectively), and they constitute layered structures with anisotropic properties and surface termination groups (–O, –F and/or –OH).[44,45] Recent research studies have shown that MXenes possess immense potential for photocatalytic applications, and $Ti_3C_2T_x$ has been introduced as an efficient co-catalyst in g-C_3N_4, $SrTiO_3$, Bi_2WO_6, $AgInS_2$ and so on to enhance their photocatalytic performance.[46–49] To date, there have been several studies on the application of MXene/BP composites in fields such as energy storage, electrocatalysis, *etc.*[50–52] However, there is still a lack of relevant research on MXene/BP composites in the photocatalysis field. According to previous studies, the MXenes possess some prominent properties for photocatalysis: (a) the efficient carrier migration in MXene systems; (b) the adjustable band gap of MXenes; (c) the outstanding light absorbance of MXenes; (d) the abundant termination surface groups with more active sites.[33,42,48,53]

Inspired by the excellent performance of MXene materials, herein, we report, for the first time, the preparation of $Ti_3C_2T_x$/TiO_2–BP nanosheet nanohybrids *via* a hydrothermal method, in which TiO_2 was formed in the hydrothermal process, which could accelerate electron transfer and provide more active sites. Multiple techniques, such as SEM, TEM, XRD, XPS, UV-Vis DRS, PL, TRPL and photoelectrochemical tests, were used to explore their crystal, morphology, and photo-electrochemical characteristics. Organic contaminants rhodamine B (RhB) and tetracycline hydrochloride (TCH) were chosen as the model pollutants for testing the visible-light photoactivity of the $Ti_3C_2T_x$/TiO_2–BP nanohybrids. Besides, density functional theory (DFT) calculations were used to study their electronic properties, including band structures, density of states, work functions, and charge density difference. This study indicates that the outstanding MXene/BP heterostructures can be potentially employed in highly efficient photocatalysis.

2. Experimental

2.1 Materials

Bulk BP crystals (purity > 99.99%) and Ti_3AlC_2 (400 mesh) were purchased from 11 Technology Co., Ltd. (China). Lithium fluoride (LiF), hydrochloric acid (HCl, 37%), RhB and TCH were all purchased from commercial corporation and used as received without further purification. Ultrapure water was used throughout the experiments.

2.2 Synthesis of photocatalysts

BP nanosheets were prepared by liquid-phase exfoliation according to previous studies with some modification,[30] namely, 30 mg of bulk BP was dispersed into 100 mL of water under nitrogen and the suspension was sonicated for 12 h. The nanosheet dispersion was finally obtained by centrifugation of the stable suspension at 3000 rpm for 3 min, and the concentration of the obtained BP nanosheet dispersion was about 0.2 mg mL^{-1}.

$Ti_3C_2T_x$ MXenes were obtained by etching the "Al" layers from the Ti_3AlC_2 phase. In detail, 2.0 g of the Ti_3AlC_2 powder was immersed in 40 mL of a mixture (6.0 g of LiF was dissolved in 100 mL of HCl (9.0 M)), and kept for 48 h at 40 °C. The residual slurry was centrifuged (6000 rpm, 3 min) and washed several times until the pH was 6.0, and then the multilayered $Ti_3C_2T_x$ was obtained. Few-layer or single layer $Ti_3C_2T_x$ sheets were prepared through the intercalation method, namely, the obtained multilayered $Ti_3C_2T_x$ was immersed in 100 mL of alcohol (as the intercalator), and continuously ultrasonicated for 3 h. Then, the mixture was centrifuged (3000 rpm, 3 min) to obtain a suspension. Finally, the few-layer or single layer $Ti_3C_2T_x$ (TC) was acquired by centrifugation of the suspension at 11 000 rpm for 5 min, and drying in a vacuum oven at 60 °C for 12 h.

The $Ti_3C_2T_x$/TiO_2–BP nanohybrids were prepared by a hydrothermal method, in detail, a certain amount of $Ti_3C_2T_x$ sheets (1 mg, 2 mg, and 3 mg) was added into 100 mL of the BP nanosheet dispersion, the mixture was stirred for 1 h, then the suspension was transferred into a 100 mL Teflon-lined stainless steel autoclave for hydrothermal treatment for 3 h at 120 °C, and the obtained $Ti_3C_2T_x$/TiO_2–BP nanohybrids were filtered and dried in a vacuum oven at 60 °C for 12 h. The nominal weight ratios of $Ti_3C_2T_x$/TiO_2 to BP were 5, 10, and 15 wt% (TCTBP-5, TCTBP-10, and TCTBP-15), respectively. For comparison purposes, the $Ti_3C_2T_x$/TiO_2 (TCT) composite was also synthesized without BP under the same conditions. The schematic illustration of the synthesis process of the $Ti_3C_2T_x$/TiO_2–BP nanohybrid is shown in Fig. 1.

2.3 Characterization

The morphology and size of the obtained samples were analysed by using field emission scanning electron microscopy (FESEM, Quanta-F20), transmission electron microscopy (TEM, Tecnai-G2 F20), and atomic force microscopy (AFM, Seiko SPA400). X-ray diffraction (XRD) patterns were obtained on a Bruker D8 Advance X-ray powder diffractometer with a Cu-Kα source. The surface composition and valence states were investigated by X-ray photoelectron spectroscopy (XPS, Thermo Fisher Scientific, UK). The UV-Vis diffuse-reflectance spectra (UV-Vis DRS) were recorded with a Varian Cary 300 spectrometer equipped with an integrating sphere. The steady-state photoluminescence (PL) spectrum and the time-resolved PL (TRPL) spectrum were measured on an Edinburgh FLS980

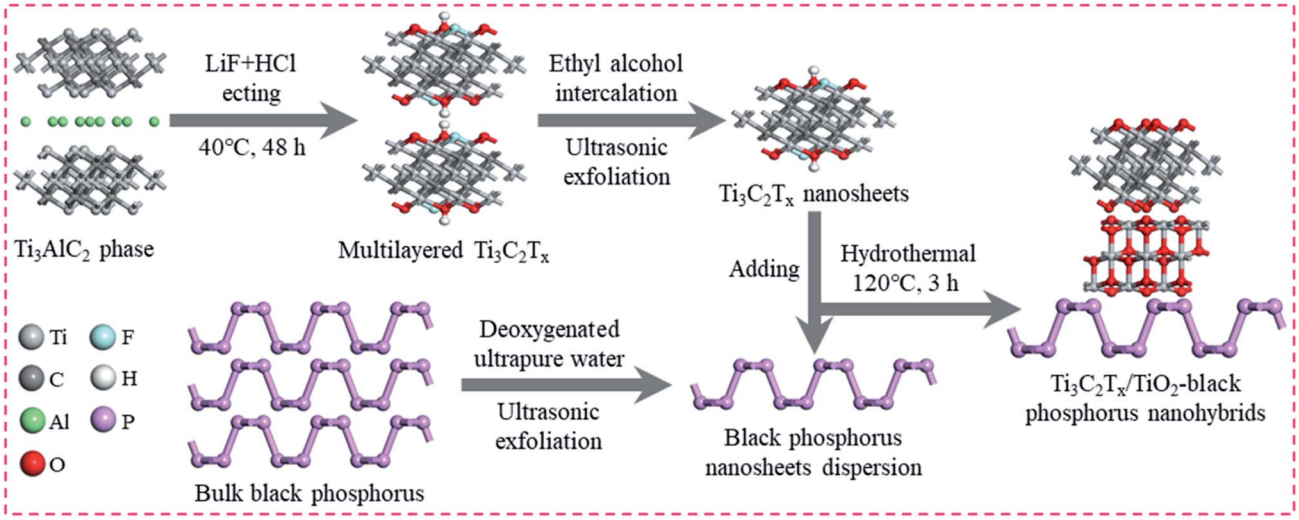

Fig. 1 Schematic illustration of the preparation process of the $Ti_3C_2T_x/TiO_2$–BP composite.

spectrophotometer. The photoelectrochemical performance test was carried out on an electrochemical workstation (CHI 660C, China) in a three-electrode system. The electron spin resonance (ESR) signals were monitored on a Bruker ER200-SRC spectrometer under visible-light illumination ($\lambda > 420$ nm). The total organic carbon (TOC) data were collected on a Shimadzu TOC-LCPH analyzer.

2.4 Photocatalytic evaluation

The photocatalytic behaviors of the as-prepared samples were studied using 20 mg L^{-1} of RhB and 10 mg L^{-1} of TCH as the contaminants. In detail, 100 mg of the sample was mixed with 100 mL of the contaminant aqueous solution. Before irradiation, the adsorption–desorption equilibrium was reached by a 30 min dark adsorption process. Then, the photodegradation tests were carried out under visible-light irradiation (a 300 W Xenon lamp was used as the light source, $\lambda > 420$ nm), every 10 min, 1 mL of solution was taken and filtered for the concentration detection using a UV-Vis spectrophotometer.

2.5 Theoretical calculations

DFT calculations were performed by employing the Cambridge Serial Total Energy Package (CASTEP) method. The exchange-correlation function was described with the generalized gradient approximation-Perdew Burke Ernzerhof (GGA-PBE) functional. Because the PBE functional may underrate the band gap of samples, the Heyd–Scuseria–Ernzerhof (HSE06) hybrid functional was employed in electronic calculations. SFC tolerance, energy cutoff and the *k*-point set were 2×10^{-6} eV $atom^{-1}$, 340 eV and $1 \times 1 \times 1$, respectively. A model of BP with 20 P atoms was tailored from the phosphorene. The model of $Ti_3C_2O_2$ was chosen for $Ti_3C_2T_x$ calculations, and it included 12 Ti, 8 C and 8 O atoms. The TiO_2 (001) surface consisting of 12 Ti and 24 O atoms was chosen for TiO_2 calculations. There were in total 20 P, 24 Ti, 8 C and 32 O atoms in the $Ti_3C_2O_2/TiO_2$–BP model. The $Ti_3C_2O_2/TiO_2$–BP model was constructed by placing the TiO_2 (001) surface 3 Å above the BP, and then placing $Ti_3C_2O_2$ 3 Å above the TiO_2 (001) surface, to form a heterogeneous structure. The valence atomic configurations are $3s^2\ 3p^3$ for P, $3d^2\ 4s^2$ for Ti, $2s^2\ 2p^2$ for C, and $2s^2\ 2p^4$ for O. A vacuum thickness of more than 15 Å was built to avoid the interference of neighboring systems along the *z*-direction for all samples (Fig. 2).

3. Results and discussion

3.1 Morphology, crystal structure, and chemical state analysis

The XRD profiles of the obtained samples are presented in Fig. 3A. Obviously, the diffraction peaks of the pristine BP nanosheets appeared at $2\theta = 17.1°$, 26.8°, 34.8°, 52.8° and 66.5° and were in agreement with the (020), (021), (040), (060) and (240) lattice planes of the orthorhombic BP phase, respectively (JCPDS no. 73-1358).[33] For $Ti_3C_2T_x$, the diffraction peaks at 6.9°, 18.8°, 28.4°, 43.6° and 61.8° correspond to the (002), (004), (006), (105) and (110) lattice planes, respectively.[54] In the hydrothermal oxidation, new peaks appeared at 25.4°, 37.9°, 48.0° and 54.0°, corresponding to the (101), (004), (200) and (105) planes of the formed anatase TiO_2 phase (JCPDS no. 21-1272) ($Ti_3C_2 + H_2O \rightarrow TiO_2 + Ti_3C_2 + C + H_2$),[54,55] which had also been confirmed by some previous studies.[55–57] In the XRD patterns of the five nanohybrids, the main characteristic peaks of both BP and $Ti_3C_2T_x/TiO_2$ were perceived, and the diffraction peak intensity varies with the content. These results demonstrated the integration of these two materials with high purity and crystallinity, and the presence of $Ti_3C_2T_x/TiO_2$ would stabilize the BP and does not affect the phase of BP.

XPS analysis was employed to accurately analyze the composition and chemical bonds in the samples. As displayed in the XPS survey spectra (Fig. 3B), the TCTBP-15 hybrid mainly contained C, O, Ti and P elements. Furthermore, the high-resolution XPS spectra of C 1s, O 1s, Ti 2p and P 2p were obtained. As displayed in Fig. 3C, the C 1s spectra were

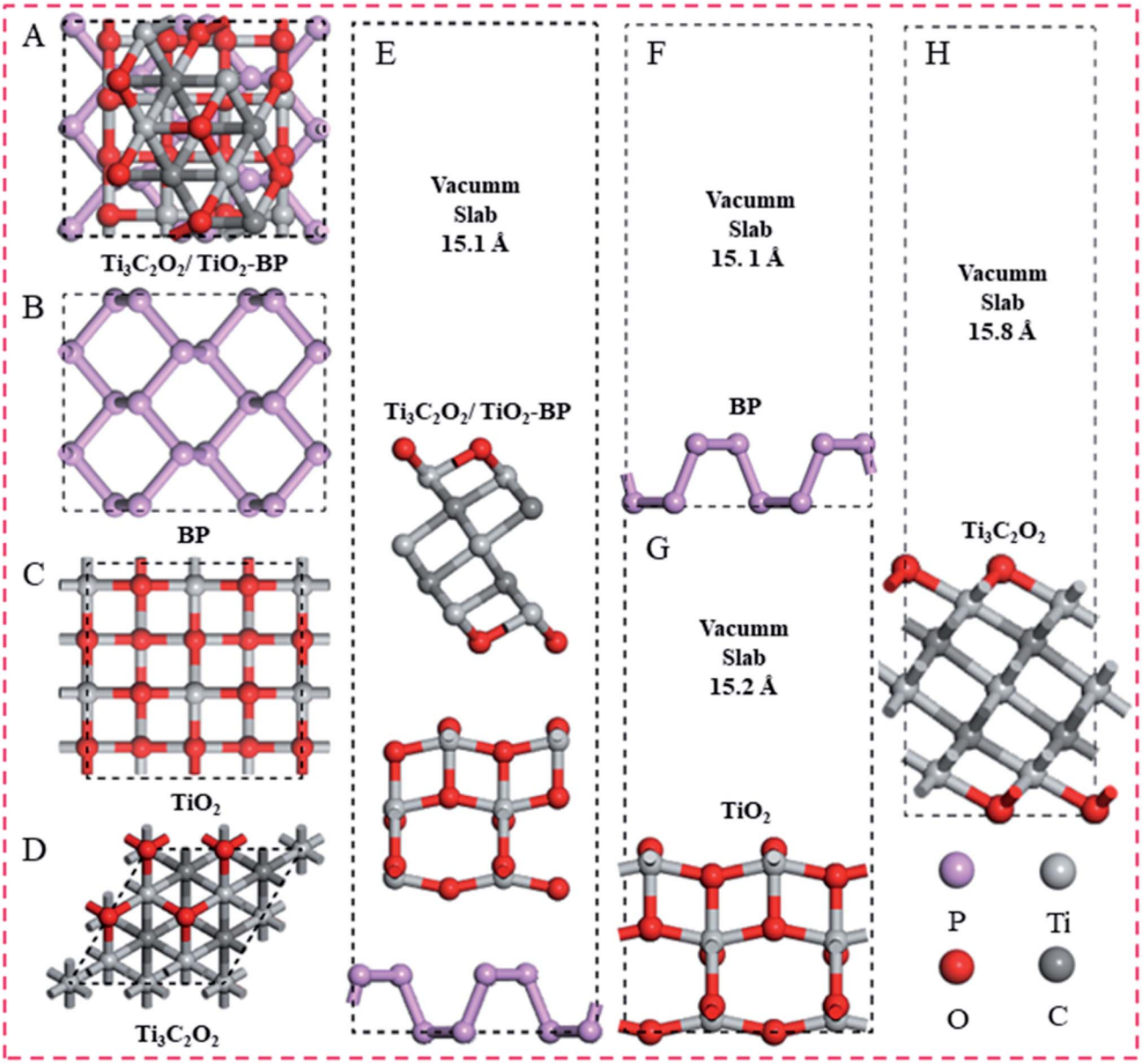

Fig. 2 Optimized geometric structures of $Ti_3C_2O_2/TiO_2$–BP, BP, TiO_2 and $Ti_3C_2O_2$, top view (A–D) and side view (E–H).

deconvoluted into five speaks at 281.95 eV, 282.85 eV, 284.70 eV, 286.17 eV and 288.57 eV, which could be assigned to C–Ti, C–Ti–O, C–C, C–O and C–F bonds, respectively.[30,55] As for the O 1s spectra (Fig. 3D), a mixture of Ti–O (529.89 eV), Ti–C–O_x (531.29 eV), Ti–O–P (532.08 eV), Ti–C–$(OH)_x$ (532.83 eV) and P–O–P (533.56 eV) can be observed.[50,51] According to the Ti 2p spectra (Fig. 3E), it was clear that the XPS spectra of Ti 2p was composed of six different peaks, the two peaks at binding energies of 459.16 eV (Ti $2p_{3/2}$) and 464.66 eV (Ti $2p_{1/2}$) were assigned to the lattice Ti–O bond in TiO_2, the two peaks at 455.3 eV (Ti $2p_{3/2}$) and 461.24 eV (Ti $2p_{1/2}$) were attributed to the lattice Ti–C bond in Ti_3C_2, the peaks at 456.64 eV (Ti $2p_{3/2}$) and 462.64 eV (Ti $2p_{1/2}$) correspond to reduced Ti ions (Ti_xO_y).[50,58] The P 2p spectrum (Fig. 3F) revealed two peaks corresponding to the P $2p_{1/2}$ (130.00 eV) and $2p_{3/2}$ (128.95 eV) orbitals. Meanwhile, the peaks at 133.03 eV and 133.85 eV correspond to the P–Ti bond and the inevitable oxidation (P_xO_y), respectively.[51,59] Based on previous studies, the formed bonds of P–Ti and Ti–O–P between BP and $Ti_3C_2T_x$ could occupy the lone pairs on BP thus largely improving the chemical stability of BP,[50,59,60] and these results were consistent with the XRD results.

The morphology of the prepared samples was investigated *via* SEM, TEM and AFM measurements. According to the SEM images (Fig. 4A), the flaky texture could be due to the BP nanosheets. Meanwhile, except BP nanosheets, bulk BP also coexisted in the BP dispersion. For the $Ti_3C_2T_x$, the multilayered $Ti_3C_2T_x$ displayed a perfect accordion-like layered structure after the Al phase was etched away (Fig. S1†). However, the delaminated $Ti_3C_2T_x$ showed a crumpled paper-like appearance, suggesting that few-layer or single layer $Ti_3C_2T_x$ sheets

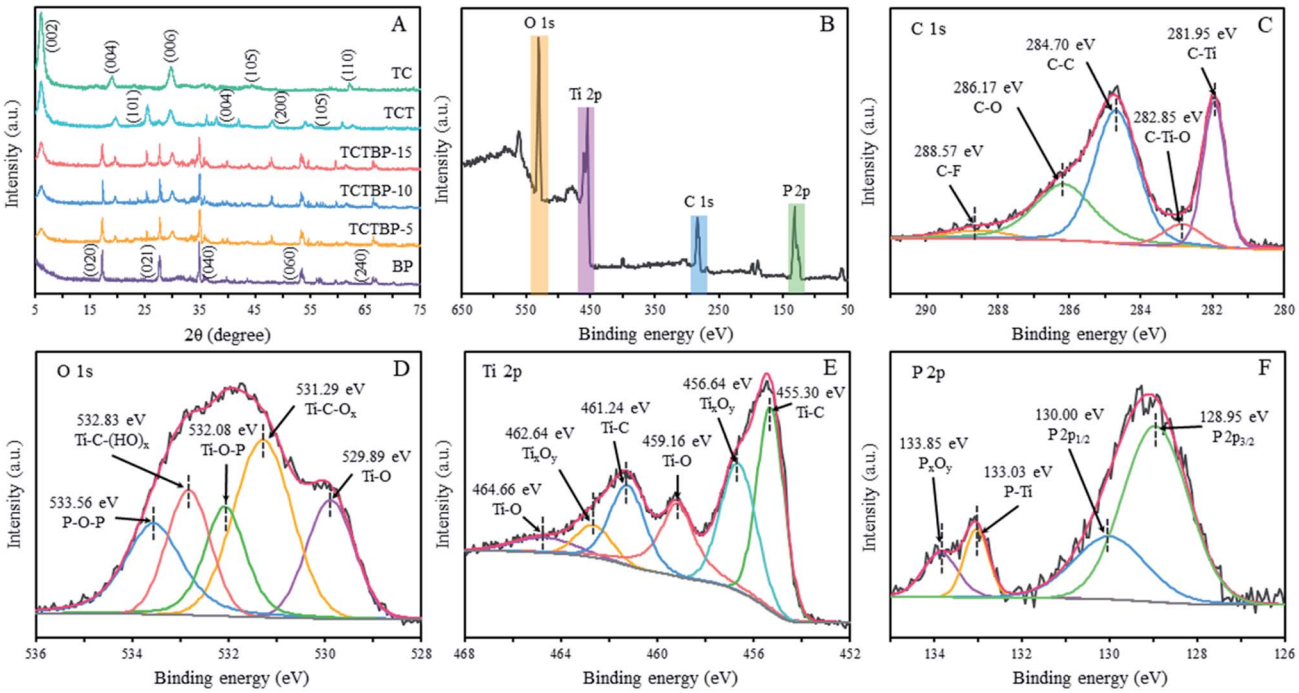

Fig. 3 XRD patterns of the as-prepared samples (A); XPS spectra of the TCTBP-15 sample (B–F).

were formed (Fig. 4C). The converted structures, from a multilayer to few-layer to even single layer, are in favor of exposing more active sites of $Ti_3C_2T_x$ and promoting the speedy electron transport.[33] Furthermore, after hydrothermal treatment of the delaminated $Ti_3C_2T_x$, some particles appeared on the surface of the $Ti_3C_2T_x$ (Fig. 4E), and they were the formed TiO_2 based on the XRD results.[55] As for the TCTBP-15 hybrid (Fig. 4H), clearly, the BP nanosheets were covered with the $Ti_3C_2T_x/TiO_2$ nanosheets. Additionally, the elemental composition and distribution of the TCTBP-15 hybrid were studied based on elemental mapping. The elemental mapping images showed that the P, Ti, O and C elements distributed evenly in the nanohybrids. The EDS analysis showed the approximate content of each element, and the results are listed in Fig. S1.† Meanwhile, the percent of $Ti_3C_2T_x$ and TiO_2 in $Ti_3C_2T_x/TiO_2$ was estimated by the increment of weight in thermogravimetric analysis (TGA) based on the previous studies (Fig. S2†),[56,57] and the value of $Ti_3C_2T_x$ and TiO_2 was 84.7 wt% and 15.3 wt%, respectively. However, it should be pointed out that part of oxygen-containing or fluorine functional groups may inevitably decompose to cause a loss of weight. Therefore, the calculated mass was an estimated value.[56,57] More details of the samples were revealed by TEM and AFM analyses, and the TEM images further verified that the BP and $Ti_3C_2T_x$ have a sheet like structure (Fig. 4B and D). Meanwhile, after the hydrothermal treatment of the $Ti_3C_2T_x$, the irregular $Ti_3C_2T_x$ sheets were converted to a regular elliptic lamellar structure (Fig. 4F), and the TEM image further verified that some TiO_2 granules with a small size of about 10–20 nm were *in situ* formed and coated uniformly on the $Ti_3C_2T_x$ layers (Fig. 4G), and the formed small TiO_2 could provide additional active sites in the photocatalytic process. As for the TCTBP-15 hybrid, it was obvious that the regular elliptic $Ti_3C_2T_x/TiO_2$ was located on the surface of BP sheets, and the "face-to-face" contact could facilitate the electron transfer from BP to $Ti_3C_2T_x$ (Fig. 4I). The HRTEM images (Fig. 4J) showed that three types of contrast fringes could be found in the TCTBP-15 hybrid; the lattice spacings of 0.261 nm, 0.214 nm and 0.236 nm correspond to the (040) plane of BP, the (012) plane of $Ti_3C_2T_x$ and the (004) plane of TiO_2, respectively. These results were consistent with those of previous studies.[39,48,54] The AFM analysis further revealed the size of samples. As displayed in Fig. 5A, the diameter of BP sheets could reach the micron scale, and their thickness was about 4.5 nm, signifying that the BP nanosheets have about nine layers.[36] The $Ti_3C_2T_x$ sheets (Fig. 5B) have nanoscale diameter, and the thickness of $Ti_3C_2T_x$ sheets was about 4.7 nm, revealing that the $Ti_3C_2T_x$ sheets have approximately three layers.[61] As for the $Ti_3C_2T_x/TiO_2$, the thickness was about 11–15 nm (Fig. S3†), which was two or three times higher than that of the $Ti_3C_2T_x$. The thickening of $Ti_3C_2T_x/TiO_2$ should be due to the shrinkage of $Ti_3C_2T_x$ and the formation of TiO_2 by hydrothermal treatment. These AFM results further revealed that the obtained samples have a few-layered nanosheet structure. Thus, the above characterization results affirmed the successful fabrication of $Ti_3C_2T_x/TiO_2$–BP nanohybrids.

3.2 Photocatalytic performance

The photocatalytic behavior of the acquired samples was estimated by the photodegradation of two common organic pollutants (RhB and TCH) under visible-light irradiation. Before the photodegradation experiments, it was studied that the adsorption–desorption equilibrium was acquired within 30

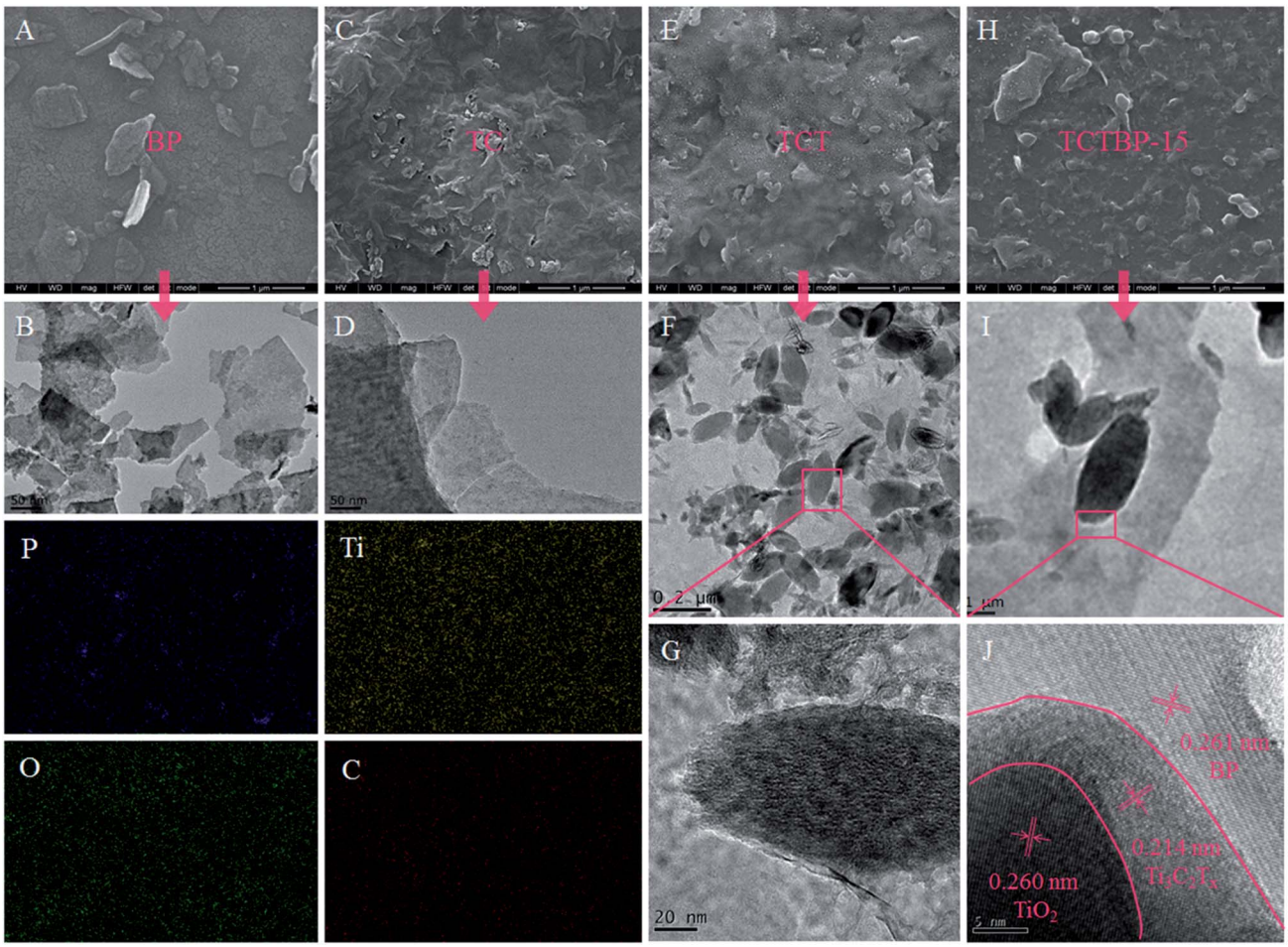

Fig. 4 SEM and TEM images of BP (A and B), TC (C and D), TCT (E–G), and TCTBP-15 (H–J); Corresponding elemental mapping images of TCTBP-15.

min. As shown in Fig. 6A and B, the $Ti_3C_2T_x/TiO_2$ showed slightly higher adsorption capacity for RhB and TCH than BP, which should be due to the $Ti_3C_2T_x/TiO_2$ nanosheets with many terminal functional groups. Compared to the pristine $Ti_3C_2T_x/TiO_2$ and BP nanosheets, the three TCTBP hybrids exhibited better adsorption capacity, which could be because of the construction of composites resulting in more porosity and active sites, thus improving the adsorption capacity of the hybrids. After the visible-light irradiation, as shown in Fig. 5A, the pristine BP nanosheets exhibited poor photodegradation activity of RhB (12.75%), which should due to the serious oxidation of pure BP nanosheets. However, $Ti_3C_2T_x/TiO_2$ (44.08%) exhibited a certain photocatalytic performance for RhB degradation; it is worth mentioning that the photodegradation of RhB by $Ti_3C_2T_x/TiO_2$ could be ascribed to the dye photosensitization effect.[54] Compared with the single photocatalysts, all of the hybrids exhibited dramatically enhanced photodegradation efficiency for RhB within 60 min, and they were in the order of TCTBP-15 (99.09%) > TCTBP-10 (98.25%) > TCTBP-5 (90.94%). For TCH degradation (Fig. 6B), the removal behavior was different to that of RhB, and the photodegradation efficiency was in the order of TCTBP-15 (92.70%) > TCTBP-10 (88.75%) > TCTBP-5 (74.00%) > TCT (10.70%) > BP (9.35%). The slightly lower photodegradation efficiency was attributed to the absence of photosensitivity in TCH, and it is also proved that the markedly increased photocatalytic activity of the composite is not caused by the dye-photosensitization phenomenon. In order to deepen the understanding of the photocatalytic behavior, the experimental results were further evaluated with a pseudo-first-order (PFO) kinetic model. The kinetic model equation can be written as follows: $-\ln(C_t/C_0) = kt$, where C_t, C_0, k, and t represent the instant concentration, initial concentration, rate constant and catalytic time, respectively. The linear fitting results are displayed in Fig. S4 and Table S1.† Obviously, the experimental results obtained for the photocatalytic process were in good agreement with the PFO model results ($R^2 > 0.96$). In terms of the rate constant, the k for RhB degradation over the TCTBP-15 nanohybrid (0.0807 min^{-1}) was about 1.22, 2.07, 9.17 and 47.47 times higher than those of TCTBP-10, TCTBP-5, TCT and BP, respectively. Meanwhile, the k for TCH degradation over TCTBP-15, TCTBP-10, TCTBP-5, TCT and BP was 0.0414, 0.0352, 0.0224, 0.0014 and 0.0013 min^{-1}, respectively. On the basis of the values of k, the TCTBP-15 nanohybrid exhibited the highest removal rate for both RhB and TCH, and the removal rate of RhB was obviously faster than that of TCH. Furthermore, the different hydrothermal treatment times and the different light source (UV-Visible light) also

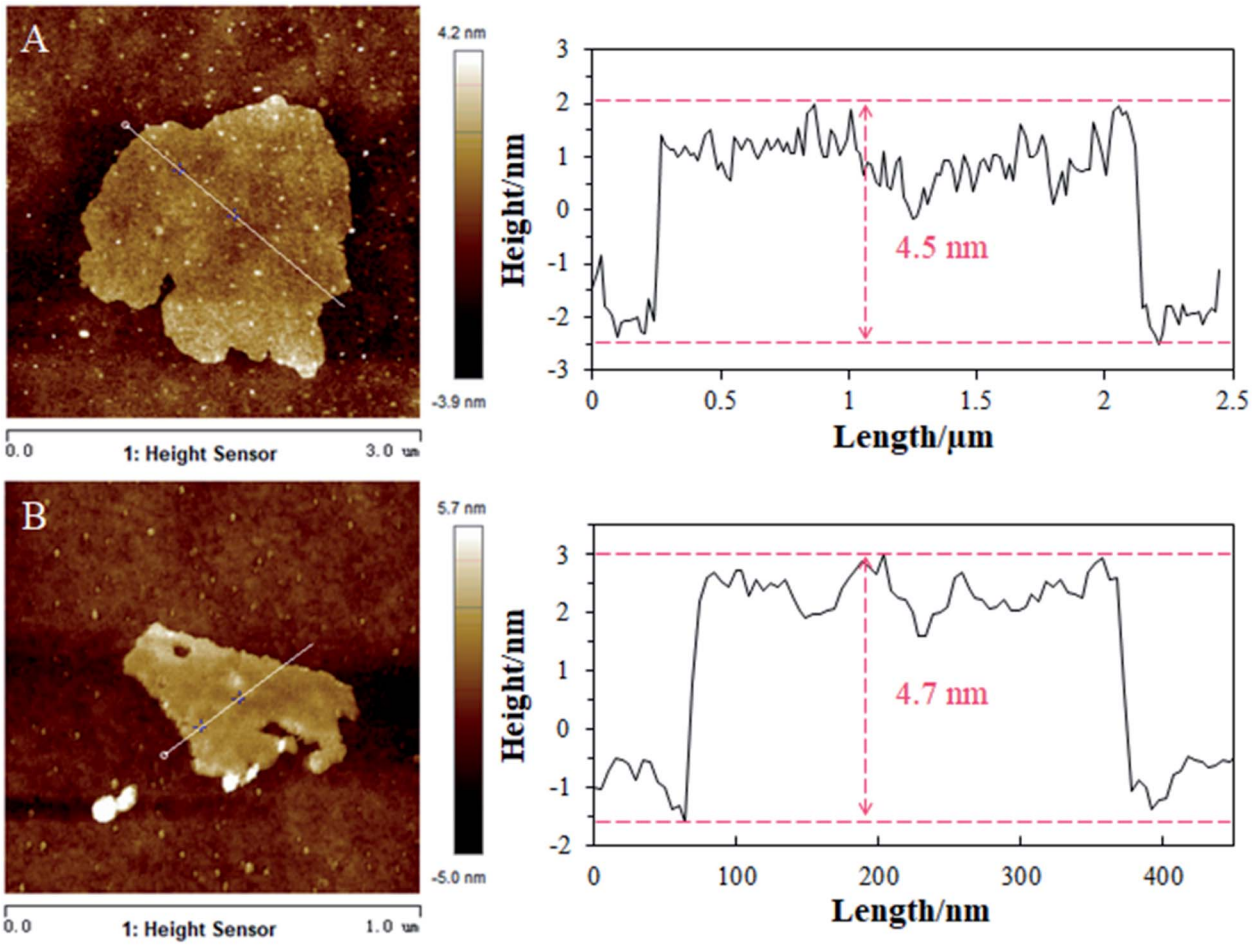

Fig. 5 AFM images and height profiles of BP (A) and TC (B).

exerted effects on the photocatalytic performance for TCH degradation, and these results are shown in Fig. S5–S7.† These results demonstrated that the $Ti_3C_2T_x/TiO_2$ decorated on the surface of BP could act as an efficient co-catalyst to increase the photocatalytic performance of BP.

As is well known, the high removal efficiency of contaminants does not imply that they had been fully degraded into CO_2 and H_2O, since intermediates would be produced during the decomposition process.[62] Herein, the TOC detection was performed over TCTBP-15 to explore the degree of mineralization of RhB and TCH. It could be seen in Fig. 6C and D that the removal rate of pollutants was slightly faster than the mineralization rate. In detail, TCTBP-15 exhibited 83.4% and 77.3% mineralization efficiency for RhB and TCH, respectively, under visible-light illumination for 60 min. Consequently, the results of TOC detection unquestionably provide enough evidence affirming the good mineralization of RhB and TCH contaminants over TCTBP-15 under visible-light irradiation.

The photostability of TCTBP-15 was investigated by performing cycle experiments for the photodegradation of contaminants (Fig. 6E). Evidently, TCTBP-15 retained almost 91.88% and 82.59% of its original activity for RhB and TCH decomposition even after four sequential cycles, manifesting that TCTBP-15 was a steady photocatalyst for the removal of environmental contaminants. A slight decrease in the degradation efficiency could be ascribed to the inevitable loss of the photocatalyst in the cycle process. In the meantime, the crystal texture of the TCTBP-15 nanohybrid had also been investigated. As displayed in Fig. 6F, the crystal structure of TCTBP-15 had no significant change after the cycle tests. Hence, in view of their outstanding photodegradation efficiency and high photostability, the synthesized TCTBP-15 nanohybrids were potential materials for practical application in environmental remediation.

3.3 Analysis of optoelectronic characteristics

To reveal the reasons for the increased photocatalytic performance, the optoelectronic characteristics of the samples were investigated. As displayed in Fig. 7A, the optical properties of the photocatalysts were investigated by UV-Vis DRS. It is obvious that the pristine BP nanosheets showed a very broad optical absorption in the UV to visible-light region, and an absorption edge at 690 nm. For $Ti_3C_2T_x$, it could be found that $Ti_3C_2T_x$ observably absorbs all photons in the 200–800 nm region, which could be due to the black color of $Ti_3C_2T_x$.[63] However, $Ti_3C_2T_x$ exhibited no clear absorption edge suggesting the metallic

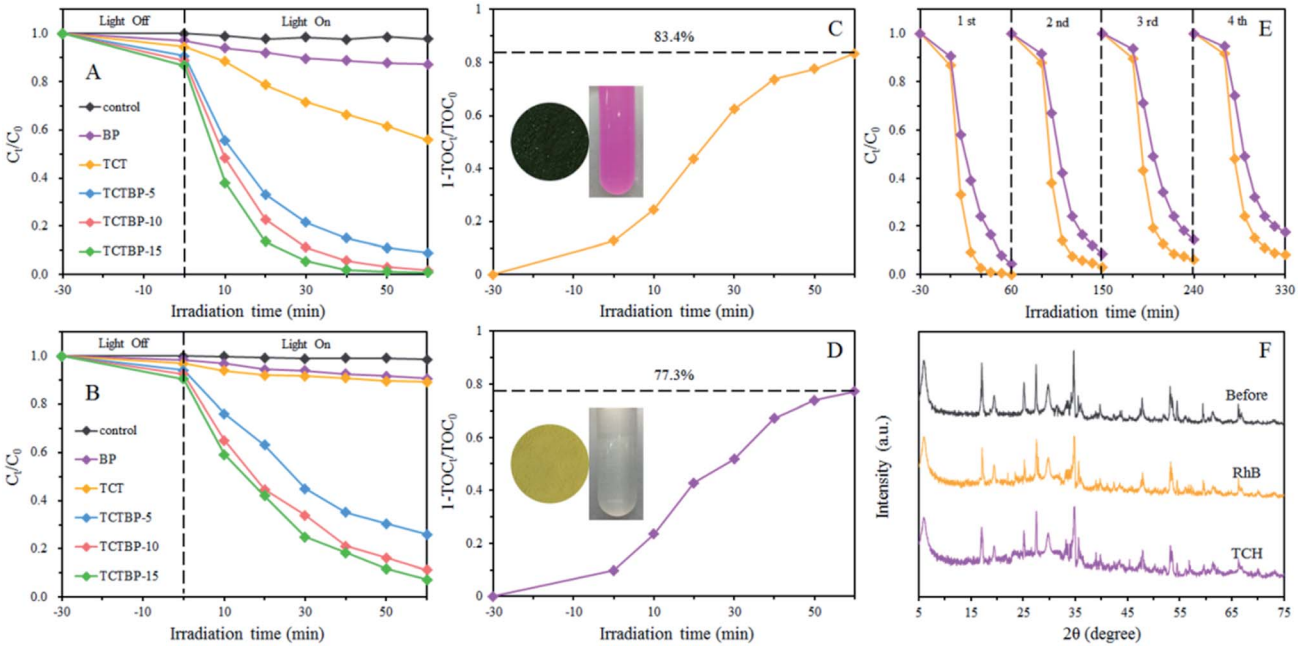

Fig. 6 The photocatalytic activities of the as-prepared samples for RhB (A) and TCH (B) degradation under visible light ($\lambda > 420$ nm); TOC removal of RhB (C) and TCH (D) by the TCTBP-15 sample; the cyclic photocatalytic experiments for the degradation of RhB (yellow line) and TCH (purple line) (E); the XRD pattern of the TCTBP-15 sample after the 4th run of cyclic photocatalytic experiments (F).

nature of $Ti_3C_2T_x$.[54] After the hydrothermal process, an absorption edge appeared at 407 nm because of the formation of anatase TiO_2.[54] As for the $Ti_3C_2T_x/TiO_2$–BP nanohybrids, the introduction of the $Ti_3C_2T_x$ could dramatically enhance the absorption of visible-light, and the absorption intensity of the $Ti_3C_2T_x/TiO_2$–BP nanohybrids gradually increased with the increase of the $Ti_3C_2T_x$ content, which would be very helpful to enhance the visible-light photocatalytic activity of the nanohybrids. In addition, the E_g of the pure BP nanosheets was estimated from the following equation: $\alpha h\nu = A(h\nu - E_g)^{n/2}$,[19] where α, h, ν and A represent the absorption coefficient, Planck constant, light frequency and a constant, respectively. According to the calculations, the E_g of BP nanosheets was about 2.0 eV (Fig. 7B). Meanwhile, the valence XPS spectra could show the energy gap from the valence band maximum (VBM) to the Fermi level (E_F) of semiconductors. As shown in Fig. 7C, the VBM position of the BP was estimated to be 1.30 eV below the Fermi level. Meanwhile, the flat band potential (E_{fb}) of BP was −0.13 eV (*vs.* NHE) based on the extrapolation of the X intercept in the MS curve,[64,65] and the MS plot showed a negative slope, suggesting the intrinsic nature of p-type BP semiconductor nanosheets (Fig. 7D), and the result was very close to those of previous studies.[66,67] As a result, the CB and VB energy levels of BP nanosheets were calculated to be −0.83 eV and 1.17 eV, respectively. The VB and CB of anatase TiO_2 could be determined based on the previous study, and they were 2.60 eV and −0.45 eV, respectively.[54]

The photoelectrochemical properties are considered to be an effective basis for evaluating the photocurrent responses and the photoexcited carrier separation of the photocatalysts. Fig. 8A displays the photocurrent intensity of the photocatalysts under visible-light illumination by depositing the catalysts on a FTO (fluorine doped tin oxide) substrate. It was obvious that the TCT sample exhibited a negligible amount of photocurrent, however, the photocurrent intensity of TCTBP-5 and TCTBP-15 nanohybrids increased evidently in comparison to that of the BP sample. Besides, the carrier transfer rate was assessed based on the arc radius in the EIS. It is widely recognized that the smaller arc in the EIS means the lower carrier migration resistance.[9,68] As displayed in Fig. 8B, the TCT sample showed the smallest arc radius in the EIS, which could be due to the metallic character of $Ti_3C_2T_x$ MXenes. Meanwhile, after the introduction of TCT, the TCTBP-5 and TCTBP-15 samples exhibited a low carrier transfer resistance compared with the BP sample. The photocurrent and EIS results suggested the existence of a heterojunction of the TCTBP nanohybrid, which was beneficial for the carrier migration process, thus efficiently reducing the recombination of photoexcited e^-–h^+ and enhancing the photocatalytic activity of the photocatalysts.

To deeply comprehend the separation and migration of the photoexcited carriers, PL detection was carried out. As depicted in Fig. 8C, although no obvious peak appeared for the TCT sample, a broad emission peak around 520 nm appeared for BP and TCTBP samples. Meanwhile, compared to pristine BP, the emission peak from the TCTBP-15 nanohybrid blue-shifts slightly and the emission intensity was quenched dramatically, indicating that the recombination of photogenerated carriers was highly restrained due to the interfacial carrier migration between BP and $Ti_3C_2T_x$.[69,70] Furthermore, for analyzing the dynamics of carrier recombination, the TRPL decay spectra of the samples were obtained (Fig. 8D). It could be found that the carrier average lifetimes of BP and TCTBP-15 were 0.33 ns and 0.72 ns, respectively, which indicated that the

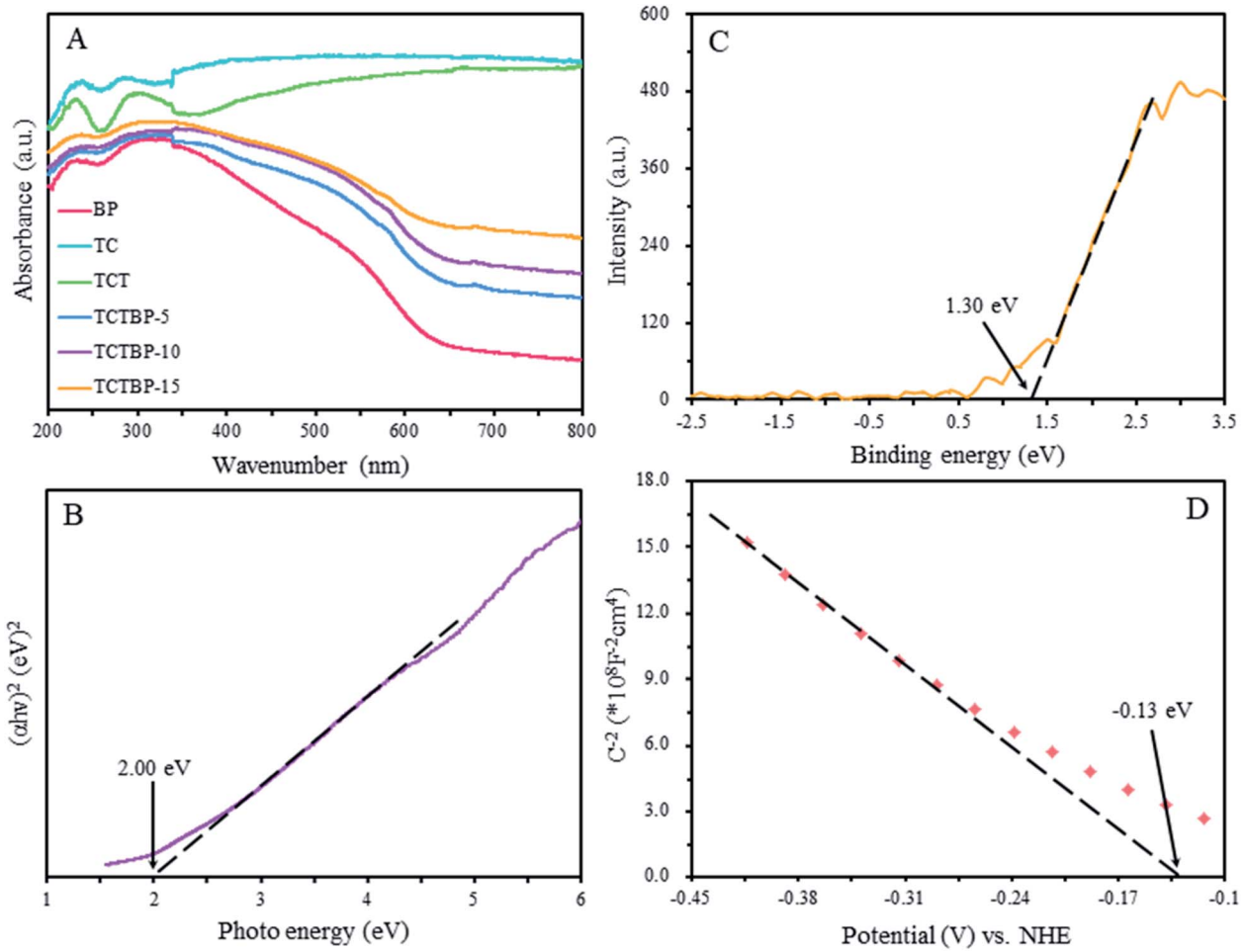

Fig. 7 UV-Vis spectrum of the as-prepared samples (A); the band gap energies of BP (B); the XPS-VB spectra of BP (C); the Mott–Schottky measurements of BP (D).

addition of $Ti_3C_2T_x/TiO_2$ was conducive to increase the carrier lifetime, and the recombination of photoexcited carrier pairs was suppressed by the heterojunction structure.[32,71] Based on the above results, in other words, the enhanced photocatalytic performance of nanohybrids for pollutants could be due to the construction of a heterojunction between $Ti_3C_2T_x/TiO_2$ and BP. The synergistic effect between each component would enhance visible-light absorption, accelerate carrier migration and separation, increase the active sites and restrain the oxidation of BP, thus improving the photocatalytic performance of nanohybrids significantly.

3.4 Theoretical calculations

Theoretical calculations are a cheap and efficient way to predict the properties of various materials. To date, diverse theoretical calculation methods have been employed in scientific research.[5,19,72,73] In this study, the electronic structures of BP, TiO_2, $Ti_3C_2O_2$ and $Ti_3C_2O_2/TiO_2$–BP were calculated based on the DFT (the model of $Ti_3C_2O_2$ was chosen for $Ti_3C_2T_x$ calculations because previous studies have indicated that the "T" element in $Ti_3C_2T_x$ is easily occupied by the "O" element after rinsing and storing under high temperature conditions,[74–76] meanwhile, it could be concluded that the $Ti_3C_2T_x$ has a prevalence of O terminations based on the XPS and EDS analysis). The optimized geometric structures of BP, TiO_2, $Ti_3C_2O_2$ and $Ti_3C_2O_2/TiO_2$–BP are shown in Fig. 2, and the lattice parameters of the samples are listed in Table 1. The lattice types of BP, TiO_2, $Ti_3C_2O_2$ and $Ti_3C_2O_2/TiO_2$–BP were all triclinic. Meanwhile, the band structures and the density of states (DOS) of the samples are shown in Fig. 9. As is well-known, the energy levels and the E_g play a vital role in deciding the photocatalytic performance of a photocatalyst. According to the calculation results, the E_g of BP and TiO_2 was 1.728 eV and 3.063 eV, respectively. These results are in close proximity to the experimental values.[31,54] Moreover, the semiconductor nature of BP and TiO_2 could be confirmed according to the corresponding band structure. As shown in Fig. 9A and C, both the valence band maximum (VBM) and the conduction band minimum (CBM) of BP were located at the *Z* point. However, the VBM and the CBM of TiO_2 were distributed at the *M* point and the *G* point, respectively. These results manifested that BP is a direct band-gap semiconductor, and TiO_2 is an indirect band-gap semiconductor, which was consistent with the experimental results.[40,54] Furthermore, the band structures of $Ti_3C_2O_2$ and $Ti_3C_2O_2/TiO_2$–BP have also been shown. Clearly, the substantial electronic states crossing the Fermi level for $Ti_3C_2O_2$ indicate its

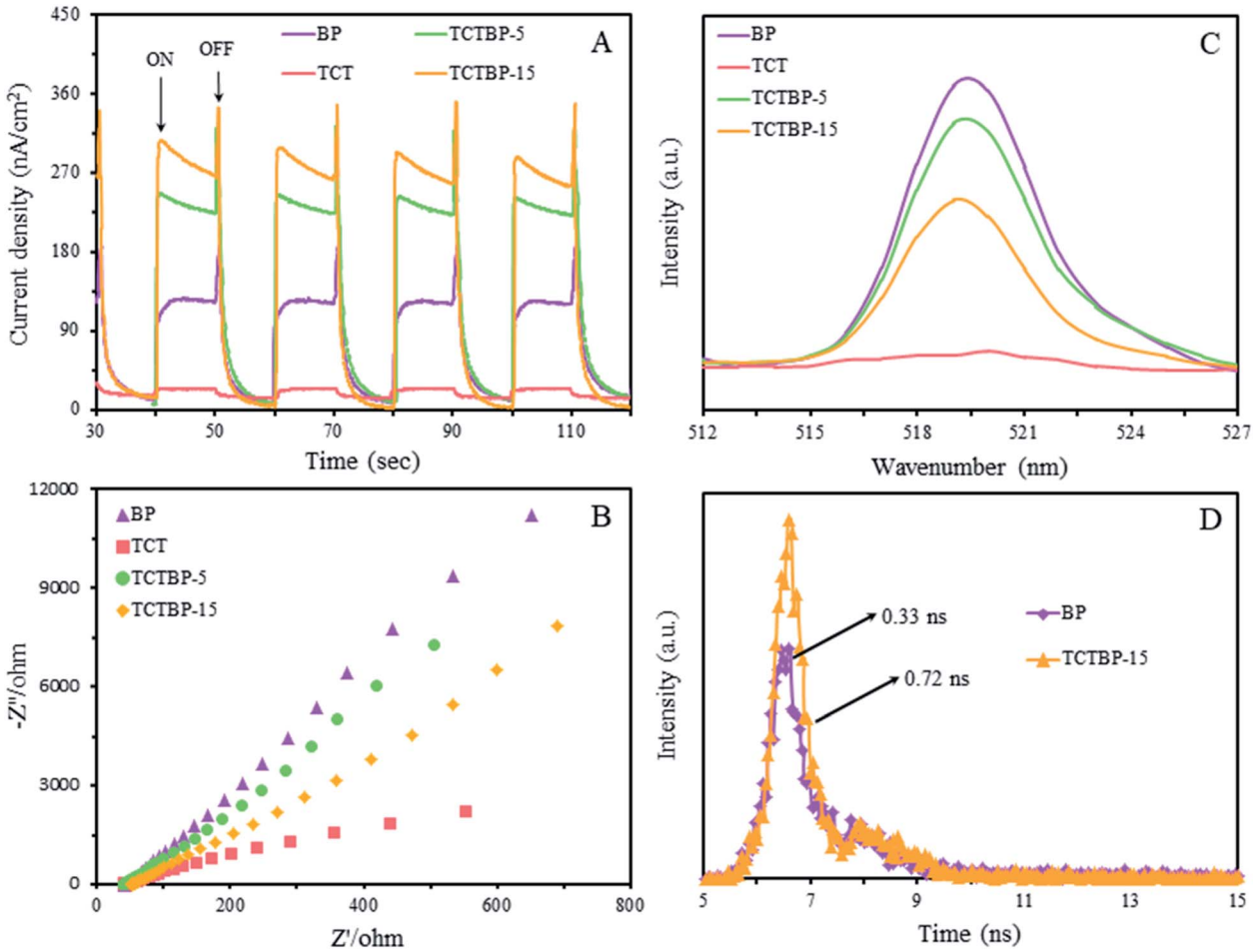

Fig. 8 The transient photocurrent (A), EIS (B), PL (C) and TRPL (D) spectra of the as-prepared samples.

Table 1 Lattice parameters of the samples

		Lengths (Å)			Angles (°)		
Samples	Lattice types	*a*	*b*	*c*	*α*	*β*	*Γ*
BP	3D triclinic	8.500	7.000	17.100	90	90	90
$Ti_3C_2O_2$	3D triclinic	6.141	6.141	22.131	90	90	120
TiO_2	3D triclinic	7.552	7.552	20.540	90	90	90
$Ti_3C_2O_2/TiO_2$–BP	3D triclinic	8.500	7.000	35.000	90	90	90

metallic characteristics, which is beneficial for electron transport (Fig. 9E).[53,63] For the $Ti_3C_2O_2/TiO_2$–BP composite (Fig. 9G), the E_g almost could not be figured out by this means which could be due to the overlap of its band structures. For their DOS, it is obvious that the DOS of BP mainly included s and p orbitals (Fig. 9B), and the DOS of TiO_2, $Ti_3C_2O_2$ and $Ti_3C_2O_2/TiO_2$–BP were composed of s, p and d orbitals (Fig. 9D, F and H). In addition, as shown in Fig. S8,† the band structure graph matched with the DOS graph. The more intense curve in the band structure graph corresponding to the higher peak value in the DOS graph signified that there are more electrons. More electrons would be beneficial to generate more carriers in the photocatalytic process.[8,19] Clearly, the band structure of $Ti_3C_2O_2/TiO_2$–BP was more intense than that of other samples, implying that it would exhibit higher photocatalytic activity. In the meantime, the TDOS and PDOS explain the orbital states of electrons in the samples. As shown in Fig. S9A,† the VBM and CBM of BP were mainly derived from P 3p and P 3s, respectively. For TiO_2 (Fig. S9B†), the VBM was mainly formed by Ti 3d orbitals, and the CBM was mainly formed by O 2s, O 2p and Ti 4s, Ti 5p orbitals. For $Ti_3C_2O_2$ (Fig. S9C†), the near-Fermi bands of $Ti_3C_2O_2$ are represented mainly by finite Ti 3d orbitals. As for the $Ti_3C_2O_2/TiO_2$–BP composite (Fig. S9D†), the DOS mainly comprises O 2s, O 2p, Ti 3d, Ti 4s, Ti 5p and P 3p orbitals.

Furthermore, the work function (WF) of a material is vital for investigating the charge transfer at the interface, and as displayed in Fig. 10, the calculated WF of BP, $Ti_3C_2O_2$, TiO_2 and $Ti_3C_2O_2/TiO_2$–BP was 4.46 eV, 4.74 eV, 5.26 eV and 4.91 eV, respectively, suggesting that the charges would easily flow from BP and $Ti_3C_2O_2$ to TiO_2 once they come into contact.[63,77] Meanwhile, the Fermi level (E_F) of samples could be converted according to the following formula (1)–(3),[28,47] where E_{VAC} is the energy of a stationary electron at the vacuum level (assumed as 0 eV). Thus the E_F of BP, $Ti_3C_2O_2$ and TiO_2 was −0.453 eV, −0.173 eV and 0.347 eV, respectively.

$$E_F\ (vs.\ \mathrm{VAC}) = E_{VAC} - \mathrm{WF} \quad (1)$$

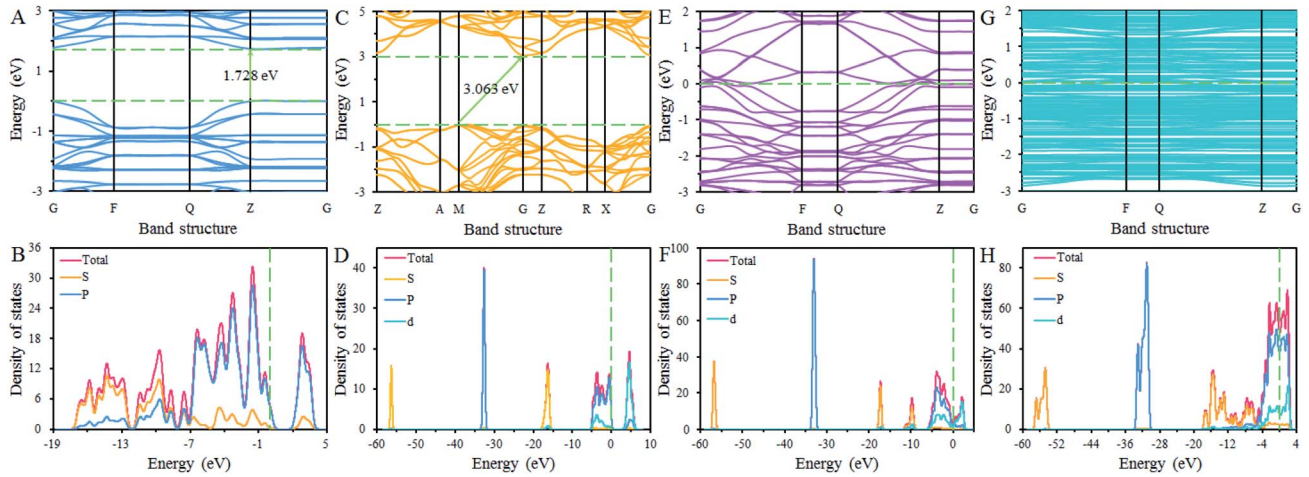

Fig. 9 Band structures and the density of states of BP (A and B), TiO_2 (C and D), $Ti_3C_2O_2$ (E and F) and $Ti_3C_2O_2/TiO_2$–BP (G and H) structures.

$$E_F\ (vs.\ \text{NHE, pH} = 0) = -4.5 - E_F\ (vs.\ \text{VAC}) \quad (2)$$

$$E_F\ (vs.\ \text{NHE, pH} = 7) = E_F\ (vs.\ \text{NHE, pH} = 0) - 0.059\text{pH} \quad (3)$$

To investigate the charge migration and separation at the $Ti_3C_2O_2/TiO_2$–BP composite, the charge density difference of $Ti_3C_2O_2/TiO_2$–BP was calculated. As displayed in Fig. 11, the blue region means charge accumulation, and the yellow region

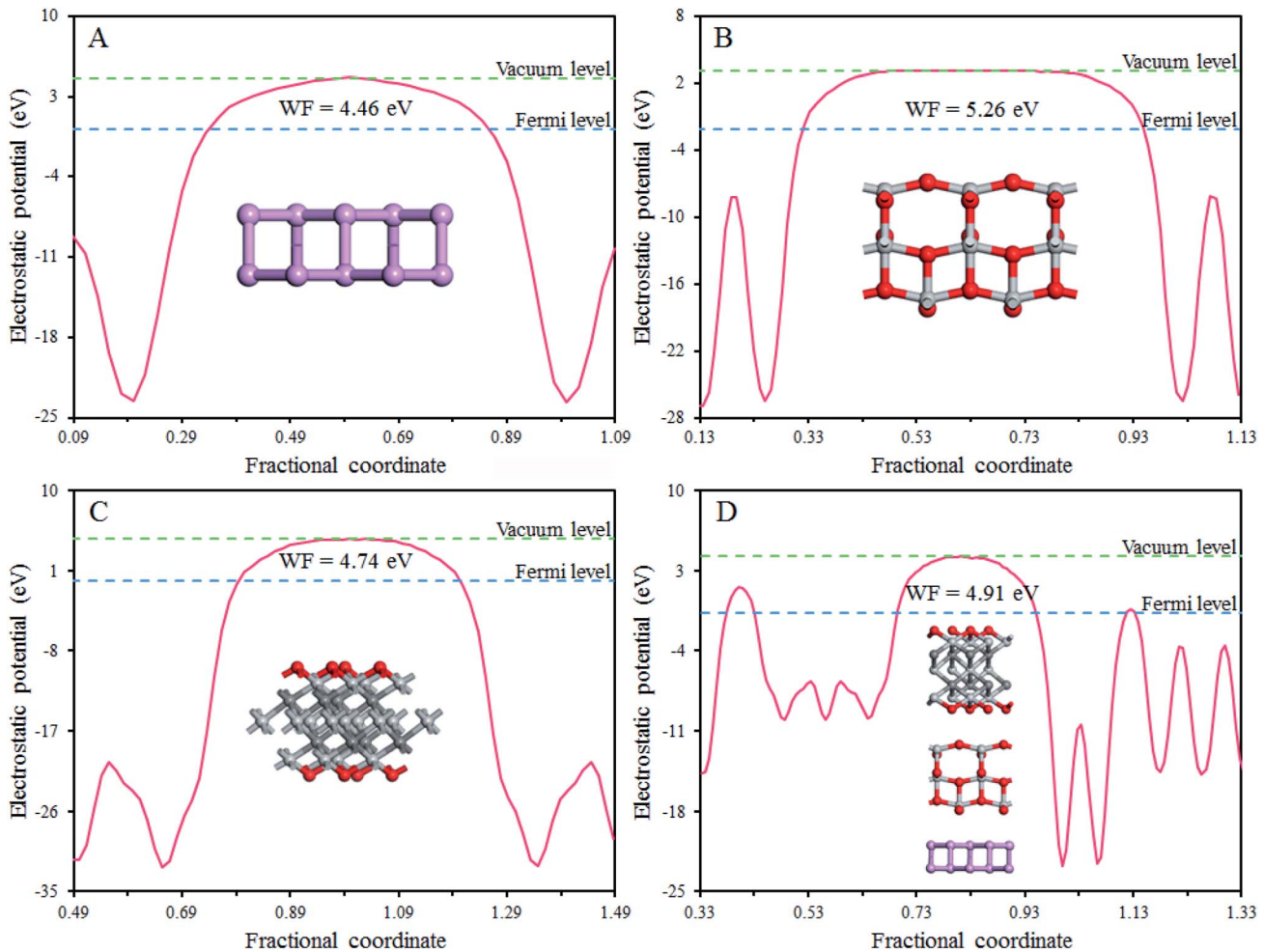

Fig. 10 Work function of BP (A), TiO_2 (B), $Ti_3C_2O_2$ (C) and $Ti_3C_2O_2/TiO_2$–BP (D) structures.

means charge depletion. For BP, TiO_2 and $Ti_3C_2O_2$ samples, their charge existed in a uniform and stable state. However, it is obvious that the charge redistribution occurred in the heterojunction, and the charge depletion is obviously more than charge accumulation, which should be due to the charge transfer occurring after the three materials came into contact. Meanwhile, the charge transfer mainly occurred at the interface region, and the direction of charge transfer was from BP to TiO_2 to $Ti_3C_2O_2$, causing a reduction of the charge concentration in BP and an increase in $Ti_3C_2O_2$. These results demonstrated the formation of interfacial internal electric fields between BP, TiO_2 and $Ti_3C_2O_2$, which would dramatically enhance the photocatalytic activity of the $Ti_3C_2O_2/TiO_2$–BP heterostructure.

3.5 Possible photocatalytic mechanism

For evaluating the photodegradation mechanism, the major active species in the photocatalytic degradation process of TCH by TCTBP-15 has been determined by scavenging experiments using *p*-benzoquinone (BQ, $^{\bullet}O_2^-$ scavengers), isopropanol (IPA, $^{\bullet}OH$ scavengers) and triethanolamine (TEA, h^+ scavengers). As displayed in Fig. 12A, the fairly small suppression effect resulting from the addition of TEA signifies that the h^+ was not regarded to take part in the TCH degradation directly. The photodegradation of TCH was markedly inhibited in the presence of BQ. The photodegradation efficiency decreased to 47.39%. This demonstrates that the $^{\bullet}O_2^-$ played a major role in the photocatalytic process. For the $^{\bullet}OH$ radical, nevertheless, efficiency decreased a little after adding IPA, indicating that the $^{\bullet}OH$ radical could not be the dominant active species. For further verifying this point, a N_2 purging experiment (excluding O_2) was also carried out. It was obvious that the photodegradation efficiency for TCH was reduced, which affirmed that the dissolved oxygen played a vital role in the photocatalytic process for the generation of radical species. It could be concluded that the $^{\bullet}O_2^-$, $^{\bullet}OH$ and h^+ worked together in the photocatalytic process, and the order of impact was $^{\bullet}O_2^- > {}^{\bullet}OH > h^+$.

To further validate the existence of these active species in the photocatalytic process, the ESR spin-trap tests were carried out by employing the TCTBP-15 sample as the photocatalyst under visible-light illumination. As displayed in Fig. 12B and C, the intensity of the DMPO-$^{\bullet}O_2^-$ and DMPO-$^{\bullet}OH$ in methanol dispersion was insignificant under dark conditions. However, under visible-light illumination, the intensity increased dramatically, indicating the generation of $^{\bullet}O_2^-$ and $^{\bullet}OH$ radicals in the photocatalytic process. Meanwhile, the $^{\bullet}O_2^-$ should derive from the reduction of O_2 because the potentials of photogenerated electrons were more negative than that for the O_2 reduction to $^{\bullet}O_2^-$ ($O_2/{}^{\bullet}O_2^-$, −0.046 eV). However, the VB potential of BP was more negative than the standard redox potential of $OH^-/{}^{\bullet}OH$ (1.99 eV),[19] and the pathway to form $^{\bullet}OH$ by the oxidation of H_2O was thermodynamically impossible.

Based on the above experimental data, a possible photocatalytic mechanism for the degradation of contaminants by the $Ti_3C_2T_x/TiO_2$–BP nanohybrid is presented in Fig. 13. According to the above results, the potentials of the CB and VB for BP were −0.83 eV and 1.17 eV, respectively. Under visible-light illumination, the photoexcited electrons transfer from the VB to the CB of BP. Afterwards, the electrons in the CB of BP would migrate to the CB of TiO_2 *via* the ultrathin layered heterojunction because of the more negative potential (−0.45 V *versus* SHE).[54] Owing to the accumulation of negative charge in TiO_2, the electrons would further move to $Ti_3C_2T_x$ because of the lower E_F of $Ti_3C_2T_x$. The electron transfer resulting from the different E_F of TiO_2 and $Ti_3C_2T_x$ would cause the formation of a depletion layer at the semiconductor/metal interface. Meanwhile, the $Ti_3C_2T_x$ possesses a lower work function than that of the TiO_2, therefore, the electrons tend to transfer from the $Ti_3C_2T_x$ to the TiO_2, leading to the energy bands of TiO_2 bend upward to form a Schottky-junction with the $Ti_3C_2T_x$ upon contact.[78] The formed Schottky barrier hindered the back-diffusion of electrons to the TiO_2 species. Meanwhile, the photoexcited electrons in BP could also migrate to the $Ti_3C_2T_x$. The obtained and photogenerated electrons rapidly shuttled to the $Ti_3C_2T_x$ surface due to the wonderful metallic conductivity (4600 ± 1100 S cm^{-1}),[54] and ultimately captured by the O_2 to generate $^{\bullet}O_2^-$ at the in-plane of $Ti_3C_2T_x$ because the E_F of $Ti_3C_2T_x$ was more negative than the potential of $O_2/{}^{\bullet}O_2^-$. Meanwhile, the generated $^{\bullet}O_2^-$ could further be reduced to produce $^{\bullet}OH$. Additionally, the $^{\bullet}OH$ could also come from the multiple electron reduction reactions ($O_2 \rightarrow H_2O_2 \rightarrow {}^{\bullet}OH$) because of the strong redox reactivity of the exposed Ti sites on the surface of $Ti_3C_2T_x$.[19,54] These strong oxidizing radicals (h^+,

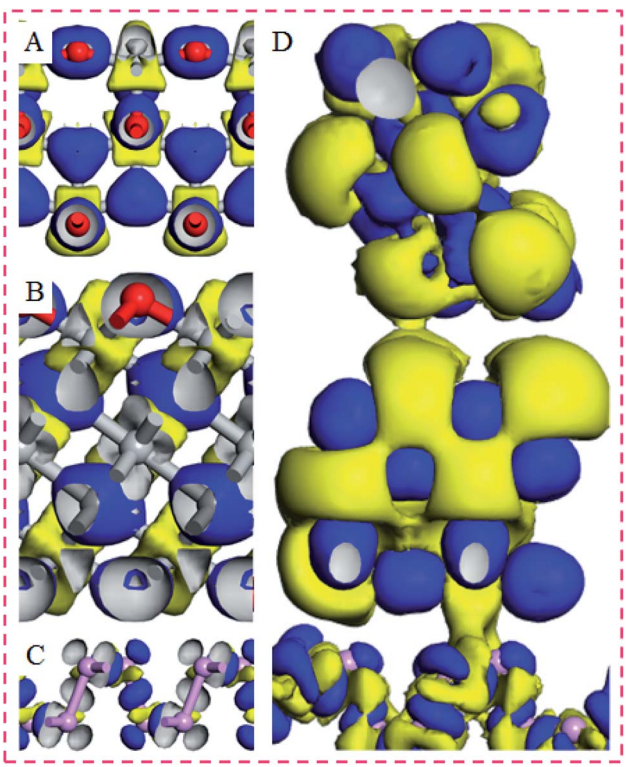

Fig. 11 The side view of the charge density difference for $Ti_3C_2O_2$ (A), TiO_2 (B), BP (C) and $Ti_3C_2O_2/TiO_2$–BP (D) structures, and the isosurface level is 0.05 e Å^{-3} for $Ti_3C_2O_2$, TiO_2 and BP, and is 0.02 e Å^{-3} for $Ti_3C_2O_2/TiO_2$–BP, and the blue and yellow areas indicate electron accumulation and depletion, respectively.

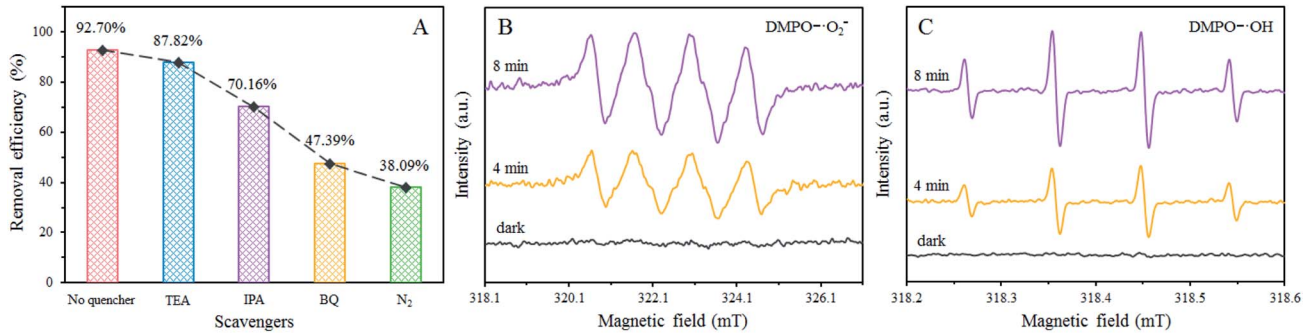

Fig. 12 Trapping experiment of radical species during the photocatalytic degradation of TCH over the TCTBP-15 sample under visible-light illumination (A); ESR spectra of radical adducts trapped by DMPO ($^{\bullet}O_2^-$ and $^{\bullet}OH$) in the TCTBP-15 sample dispersion in the dark and under visible light illumination: in methanol dispersion for DMPO-$^{\bullet}O_2^-$ (B); in aqueous dispersion for DMPO-$^{\bullet}OH$ (C).

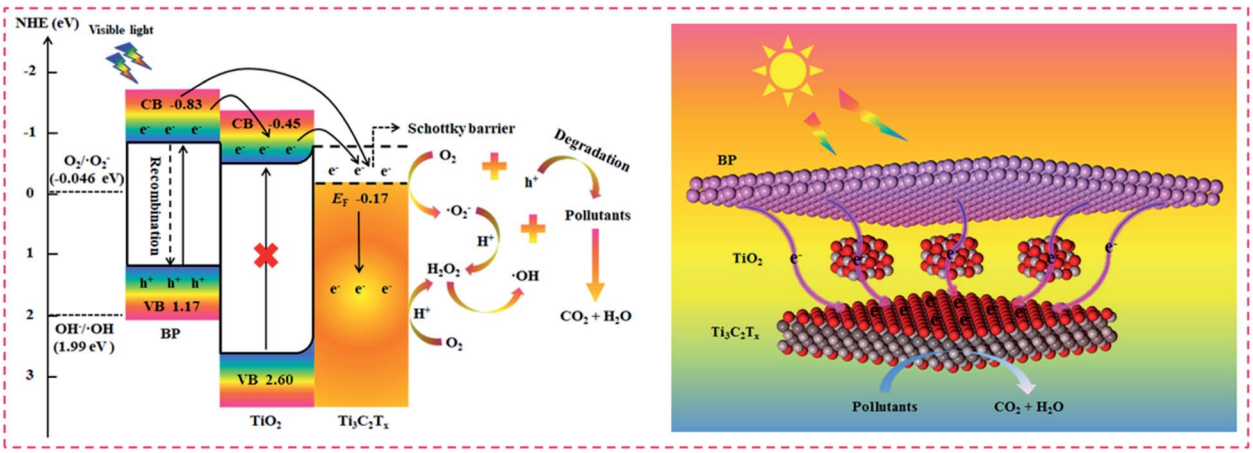

Fig. 13 Schematic diagram for possible charge separation and the photocatalytic mechanism of the $Ti_3C_2T_x/TiO_2$–BP composite.

$^{\bullet}O_2^-$, and $^{\bullet}OH$) finally degraded organic contaminants into CO_2, H_2O or others. The major possible reactions are described as follows:

$$BP + \text{visible light} \rightarrow BP\ (e^-/h^+) \rightarrow TiO_2\ (e^-) \rightarrow Ti_3C_2T_x\ (e^-) \quad (4)$$

$$Ti_3C_2T_x\ (e^-) + O_2 \rightarrow {}^{\bullet}O_2^- \quad (5)$$

$${}^{\bullet}O_2^- + H^+ \rightarrow {}^{\bullet}OOH \quad (6)$$

$${}^{\bullet}OOH + H^+ + e^- \rightarrow H_2O_2 \quad (7)$$

$$O_2 + 2H^+ + 2e^- \rightarrow H_2O_2 \quad (8)$$

$$H_2O_2 + e^- \rightarrow {}^{\bullet}OH + OH^- \quad (9)$$

$${}^{\bullet}O_2^- + {}^{\bullet}OH + h^+ + \text{pollutants} \rightarrow \text{degradation products} \quad (10)$$

4. Conclusions

In summary, novel $Ti_3C_2T_x/TiO_2$–BP nanohybrids were constructed by a hydrothermal method. The photodegradation experiments indicated that the optimized TCTBP-15 nanohybrid exhibited enhanced visible-light photocatalytic activity towards degradation of contaminants RhB and TCH, which were 47.47 and 31.85 fold higher than that of pure BP, respectively. Various characterization techniques manifested that the enhanced photocatalytic activity was attributed to the synergistic effect and the Schottky junction formed between BP and $Ti_3C_2T_x/TiO_2$, which significantly improved the physicochemical and optoelectronic properties, increased visible-light absorption, prolonged the photoexcited electron lifetime, accelerated the photoinduced electron transfer and hindered the e^-–h^+ pair recombination, enhanced the active sites and suppressed the oxidation of BP. Meanwhile, the theoretical calculations further verified these merits of $Ti_3C_2T_x/TiO_2$–BP nanohybrids. Furthermore, the mechanism analysis affirmed that the active species $^{\bullet}O_2^-$ played a leading role in the photodegradation system. We believe that this work will provide some new inspiration in utilizing MXenes as co-catalysts to enhance the activity of BP for environmental remediation and some other applications.

Conflicts of interest

There are no conflicts to declare.

Acknowledgements

The study was financially supported by the Program for Changjiang Scholars and Innovative Research Team in University (IRT-13R17), the National Natural Science Foundation of China (51979103, 51909085, 51679085, 51521006, 51508177, and 51579096), the Fundamental Research Funds for the Central Universities of China (531107050930), the Funds of Hunan Science and Technology Innovation Project (2018RS3115 and 2019RS3012), and China Postdoctoral Science Foundation Funded Project (2018M642977). The special support for the application of computing science from High-performance Computing Center of Guangxi University is acknowledged.

References

1 Y. Liu, M. Cheng, Z. Liu, G. Zeng, H. Zhong, M. Chen, C. Zhou, W. Xiong, B. Shao and B. Song, *Chemosphere*, 2019, **236**, 124387.
2 S.-H. Turren-Cruz, A. Hagfeldt and M. Saliba, *Science*, 2018, **362**, 449–453.
3 C. W. Lee, N. H. Cho, S. W. Im, M. S. Jee, Y. J. Hwang, B. K. Min and K. T. Nam, *J. Mater. Chem. A*, 2018, **6**, 14043–14057.
4 S. Wu, H. Liu, C. Yang, X. Li, Y. Lin, K. Yin, J. Sun, Q. Teng, C. Du and Y. Zhong, *Chem. Eng. J.*, 2019, 123683, DOI: 10.1016/j.cej.2019.123683.
5 B. Shao, Z. Liu, G. Zeng, Y. Liu, X. Yang, C. Zhou, M. Chen, Y. Liu, Y. Jiang and M. Yan, *J. Hazard. Mater.*, 2019, **362**, 318–326.
6 M. Freitag, J. Teuscher, Y. Saygili, X. Zhang, F. Giordano, P. Liska, J. Hua, S. M. Zakeeruddin, J.-E. Moser, M. Grätzel and A. Hagfeldt, *Nat. Photonics*, 2017, **11**, 372–378.
7 A. Fujishima and K. Honda, *Nature*, 1972, **238**, 37–38.
8 B. Shao, X. Liu, Z. Liu, G. Zeng, Q. Liang, C. Liang, Y. Cheng, W. Zhang, Y. Liu and S. Gong, *Chem. Eng. J.*, 2019, **368**, 730–745.
9 B. Shao, Z. Liu, G. Zeng, Z. Wu, Y. Liu, M. Cheng, M. Chen, Y. Liu, W. Zhang and H. Feng, *ACS Sustainable Chem. Eng.*, 2018, **6**, 16424–16436.
10 T. Wu, X. Liu, Y. Liu, M. Cheng, Z. Liu, G. Zeng, B. Shao, Q. Liang, W. Zhang, Q. He and W. Zhang, *Coord. Chem. Rev.*, 2020, **403**, 213097.
11 J. Wang, L. Tang, G. Zeng, Y. Deng, Y. Liu, L. Wang, Y. Zhou, Z. Guo, J. Wang and C. Zhang, *Appl. Catal., B*, 2017, **209**, 285–294.
12 S. Chattopadhyay, S. Bysakh, P. M. Mishra and G. De, *Langmuir*, 2019, **35**, 14364–14375.
13 V. Chernikova, O. Yassine, O. Shekhah, M. Eddaoudi and K. N. Salama, *J. Mater. Chem. A*, 2018, **6**, 5550–5554.
14 Y. Zhao, X. Zhang, X. Jia, G. I. N. Waterhouse, R. Shi, X. Zhang, F. Zhan, Y. Tao, L.-Z. Wu, C.-H. Tung, D. O'Hare and T. Zhang, *Adv. Energy Mater.*, 2018, **8**, 1703585.
15 J. Li, X. Gao, B. Liu, Q. Feng, X.-B. Li, M.-Y. Huang, Z. Liu, J. Zhang, C.-H. Tung and L.-Z. Wu, *J. Am. Chem. Soc.*, 2016, **138**, 3954–3957.
16 Y.-W. Zheng, B. Chen, P. Ye, K. Feng, W. Wang, Q.-Y. Meng, L.-Z. Wu and C.-H. Tung, *J. Am. Chem. Soc.*, 2016, **138**, 10080–10083.
17 K. Domanski, E. A. Alharbi, A. Hagfeldt, M. Grätzel and W. Tress, *Nat. Energy*, 2018, **3**, 61–67.
18 X. Zhang, A. Chen, Z. Zhang, M. Jiao and Z. Zhou, *J. Mater. Chem. A*, 2018, **6**, 11446–11452.
19 B. Shao, X. Liu, Z. Liu, G. Zeng, W. Zhang, Q. Liang, Y. Liu, Q. He, X. Yuan, D. Wang, S. Luo and S. Gong, *Chem. Eng. J.*, 2019, **374**, 479–493.
20 Q. Liang, X. Liu, G. Zeng, Z. Liu, L. Tang, B. Shao, Z. Zeng, W. Zhang, Y. Liu, M. Cheng, W. Tang and S. Gong, *Chem. Eng. J.*, 2019, **372**, 429–451.
21 E. N. El Sawy and V. I. Birss, *ACS Appl. Mater. Interfaces*, 2018, **10**, 3459–3469.
22 S.-H. Turren-Cruz, M. Saliba, M. T. Mayer, H. Juárez-Santiesteban, X. Mathew, L. Nienhaus, W. Tress, M. P. Erodici, M.-J. Sher, M. G. Bawendi, M. Grätzel, A. Abate, A. Hagfeldt and J.-P. Correa-Baena, *Energy Environ. Sci.*, 2018, **11**, 78–86.
23 Y. Zhao, G. I. N. Waterhouse, G. Chen, X. Xiong, L.-Z. Wu, C.-H. Tung and T. Zhang, *Chem. Soc. Rev.*, 2019, **48**, 1972–2010.
24 Z. Shen, S. Sun, W. Wang, J. Liu, Z. Liu and J. C. Yu, *J. Mater. Chem. A*, 2015, **3**, 3285–3288.
25 R. Gui, H. Jin, Y. Sun, X. Jiang and Z. Sun, *J. Mater. Chem. A*, 2019, **7**, 25712–25771.
26 M. Zhu, C. Zhai, M. Fujitsuka and T. Majima, *Appl. Catal., B*, 2018, **221**, 645–651.
27 P. Vishnoi, U. Gupta, R. Pandey and C. N. R. Rao, *J. Mater. Chem. A*, 2019, **7**, 6631–6637.
28 Y. Chen, T. Shi, P. Liu, X. Ma, L. Shui, C. Shang, Z. Chen, X. Wang, K. Kempa and G. Zhou, *J. Mater. Chem. A*, 2018, **6**, 19167–19175.
29 T. Song, G. Zeng, P. Zhang, T. Wang, A. Ali, S. Huang and H. Zeng, *J. Mater. Chem. A*, 2019, **7**, 503–512.
30 P. Qiu, C. Xu, N. Zhou, H. Chen and F. Jiang, *Appl. Catal., B*, 2018, **221**, 27–35.
31 J. Ran, W. Guo, H. Wang, B. Zhu, J. Yu and S. Z. Qiao, *Adv. Mater.*, 2018, **30**, e1800128.
32 M. Wen, J. Wang, R. Tong, D. Liu, H. Huang, Y. Yu, Z. K. Zhou, P. K. Chu and X. F. Yu, *Adv. Sci.*, 2019, **6**, 1801321.
33 Y.-J. Yuan, P. Wang, Z. Li, Y. Wu, W. Bai, Y. Su, J. Guan, S. Wu, J. Zhong, Z.-T. Yu and Z. Zou, *Appl. Catal., B*, 2019, **242**, 1–8.
34 X. Ling, H. Wang, S. Huang, F. Xia and M. S. Dresselhaus, *Proc. Natl. Acad. Sci. U. S. A.*, 2015, **112**, 4523–4530.
35 X. Zhu, T. Zhang, Z. Sun, H. Chen, J. Guan, X. Chen, H. Ji, P. Du and S. Yang, *Adv. Mater.*, 2017, **29**, 1605776.
36 Q. Zhang, S. Huang, J. Deng, D. T. Gangadharan, F. Yang, Z. Xu, G. Giorgi, M. Palummo, M. Chaker and D. Ma, *Adv. Funct. Mater.*, 2019, 1902486, DOI: 10.1002/adfm.201902486.
37 D. A. Reddy, E. H. Kim, M. Gopannagari, Y. Kim, D. P. Kumar and T. K. Kim, *Appl. Catal., B*, 2019, **241**, 491–498.
38 Y. Liu, M. Zhou, W. Zhang, K. Chen, A. Mei, Y. Zhang and W. Chen, *Nanoscale*, 2019, **11**, 5674–5683.

39 M. Zhu, Z. Sun, M. Fujitsuka and T. Majima, *Angew. Chem., Int. Ed.*, 2018, **57**, 2160–2164.
40 J. Hu, D. Chen, Z. Mo, N. Li, Q. Xu, H. Li, J. He, H. Xu and J. Lu, *Angew. Chem., Int. Ed.*, 2019, **58**, 2073–2077.
41 N. Michael, K. Murat, P. Volker, L. Jun, N. Junjie, H. Min, H. Lars, G. Yury and M. W. Barsoum, *Adv. Mater.*, 2011, **23**, 4248–4253.
42 J. Peng, X. Chen, W.-J. Ong, X. Zhao and N. Li, *Chem*, 2019, **5**, 18–50.
43 X. Zhang, Z. Zhang and Z. Zhou, *J. Energy Chem.*, 2018, **27**, 73–85.
44 Y. Sun, D. Jin, Y. Sun, X. Meng, Y. Gao, Y. Dall'Agnese, G. Chen and X.-F. Wang, *J. Mater. Chem. A*, 2018, **6**, 9124–9131.
45 V. M. Hong Ng, H. Huang, K. Zhou, P. S. Lee, W. Que, J. Z. Xu and L. B. Kong, *J. Mater. Chem. A*, 2017, **5**, 3039–3068.
46 Y. Xu, S. Wang, J. Yang, B. Han, R. Nie, J. Wang, Y. Dong, X. Yu, J. Wang and H. Jing, *J. Mater. Chem. A*, 2018, **6**, 15213–15220.
47 S. Cao, B. Shen, T. Tong, J. Fu and J. Yu, *Adv. Funct. Mater.*, 2018, **28**, 1800136.
48 J. Qin, X. Hu, X. Li, Z. Yin, B. Liu and K.-h. Lam, *Nano Energy*, 2019, **61**, 27–35.
49 C. Peng, P. Wei, X. Li, Y. Liu, Y. Cao, H. Wang, H. Yu, F. Peng, L. Zhang, B. Zhang and K. Lv, *Nano Energy*, 2018, **53**, 97–107.
50 R. Meng, J. Huang, Y. Feng, L. Zu, C. Peng, L. Zheng, L. Zheng, Z. Chen, G. Liu, B. Chen, Y. Mi and J. Yang, *Adv. Energy Mater.*, 2018, **8**, 1801514.
51 X.-D. Zhu, Y. Xie and Y.-T. Liu, *J. Mater. Chem. A*, 2018, **6**, 21255.
52 X. Zhang, Z. Zhang, J. Li, X. Zhao, D. Wu and Z. Zhou, *J. Mater. Chem. A*, 2017, **5**, 12899–12903.
53 Z. Zeng, Y. Yan, J. Chen, P. Zan, Q. Tian and P. Chen, *Adv. Funct. Mater.*, 2019, **29**, 1806500.
54 H. Wang, Y. Wu, T. Xiao, X. Yuan, G. Zeng, W. Tu, S. Wu, H. Y. Lee, Y. Z. Tan and J. W. Chew, *Appl. Catal., B*, 2018, **233**, 213–225.
55 C. Peng, X. Yang, Y. Li, H. Yu, H. Wang and F. Peng, *ACS Appl. Mater. Interfaces*, 2016, **8**, 6051–6060.
56 C. Yang, Y. Liu, X. Sun, Y. Zhang, L. Hou, Q. Zhang and C. Yuan, *Electrochim. Acta*, 2018, **271**, 165–172.
57 T. Xu, J. Wang, Y. Cong, S. Jiang, Q. Zhang, H. Zhu, Y. Li and X. Li, *Chin. Chem. Lett.*, 2019, DOI: 10.1016/j.cclet.2019.11.038.
58 Y. Li, Z. Yin, G. Ji, Z. Liang, Y. Xue, Y. Guo, J. Tian, X. Wang and H. Cui, *Appl. Catal., B*, 2019, **246**, 12–20.
59 T. Song, H. Chen, Z. Li, Q. Xu, H. Liu, Y. Wang and Y. Xia, *Adv. Funct. Mater.*, 2019, **29**, 1900535.
60 J. Mei, Y. Zhang, T. Liao, X. Peng, G. A. Ayoko and Z. Sun, *Energy Storage Materials*, 2019, **19**, 424–431.
61 A. Lipatov, M. Alhabeb, M. R. Lukatskaya, A. Boson, Y. Gogotsi and A. Sinitskii, *Adv. Electron. Mater.*, 2016, **2**, 1600255.
62 Z. Peng, X. Liu, W. Zhang, Z. Zeng, Z. Liu, C. Zhang, Y. Liu, B. Shao, Q. Liang, W. Tang and X. Yuan, *Environ. Int.*, 2020, **134**, 105298.
63 J. Ran, G. Gao, F. T. Li, T. Y. Ma, A. Du and S. Z. Qiao, *Nat. Commun.*, 2017, **8**, 13907.
64 Z. Jiang, W. Wan, H. Li, S. Yuan, H. Zhao and P. K. Wong, *Adv. Mater.*, 2018, **30**, 1706108.
65 M. Zhu, X. Cai, M. Fujitsuka, J. Zhang and T. Majima, *Angew. Chem., Int. Ed.*, 2017, **56**, 2064–2068.
66 B. Tian, B. Tian, B. Smith, M. C. Scott, Q. Lei, R. Hua, Y. Tian and Y. Liu, *Proc. Natl. Acad. Sci. U. S. A.*, 2018, **115**, 4345–4350.
67 B. Tian, B. Tian, B. Smith, M. C. Scott, R. Hua, Q. Lei and Y. Tian, *Nat. Commun.*, 2018, **9**, 1397.
68 C. Zhou, C. Lai, D. Huang, G. Zeng, C. Zhang, M. Cheng, L. Hu, J. Wan, W. Xiong, M. Wen, X. Wen and L. Qin, *Appl. Catal., B*, 2018, **220**, 202–210.
69 J.-H. Zhao, L.-W. Liu, K. Li, T. Li and F.-T. Liu, *CrystEngComm*, 2019, **21**, 2416–2421.
70 B. Wang, J. Iocozzia, M. Zhang, M. Ye, S. Yan, H. Jin, S. Wang, Z. Zou and Z. Lin, *Chem. Soc. Rev.*, 2019, **48**, 4854–4891.
71 S. Yao, X. Zhang, A. Chen, Z. Zhang, M. Jiao and Z. Zhou, *J. Mater. Chem. A*, 2019, **7**, 19290–19296.
72 Z. Liu, B. Shao, G. Zeng, M. Chen, Z. Li, Y. Liu, Y. Jiang, H. Zhong, Y. Liu and M. Yan, *Chemosphere*, 2018, **210**, 922–930.
73 A. Agresti, A. Pazniak, S. Pescetelli, A. Di Vito, D. Rossi, A. Pecchia, M. Auf der Maur, A. Liedl, R. Larciprete, D. V. Kuznetsov, D. Saranin and A. Di Carlo, *Nat. Mater.*, 2019, **18**, 1228–1234.
74 X. Zhang, J. Lei, D. Wu, X. Zhao, Y. Jing and Z. Zhou, *J. Mater. Chem. A*, 2016, **4**, 4871–4876.
75 J.-C. Lei, X. Zhang and Z. Zhou, *Front. Phys.*, 2015, **10**, 276–286.
76 Y. Xie, M. Naguib, V. N. Mochalin, M. W. Barsoum, Y. Gogotsi, X. Yu, K.-W. Nam, X.-Q. Yang, A. I. Kolesnikov and P. R. C. Kent, *J. Am. Chem. Soc.*, 2014, **136**, 6385–6394.
77 H. Wang, Y. Sun, Y. Wu, W. Tu, S. Wu, X. Yuan, G. Zeng, Z. J. Xu, S. Li and J. W. Chew, *Appl. Catal., B*, 2019, **245**, 290–301.
78 P. Lin, J. Shen, X. Yu, Q. Liu, D. Li and H. Tang, *Ceram. Int.*, 2019, **45**, 24656–24663.